PROCEEDINGS OF THE SEVENTEENTH LUNAR AND PLANETARY SCIENCE CONFERENCE, PART 2
JOURNAL OF GEOPHYSICAL RESEARCH, VOL. 92, NO. B4, PAGES E387-E395, MARCH 30, 1987

Global Petrologic Variations on the Moon: A Ternary-Diagram Approach

PHILIP A. DAVIS AND PAUL D. SPUDIS

U. S. Geological Survey, Flagstaff, Arizona

A ternary-diagram approach for determination of global petrologic variations on the lunar surface is presented that incorporates valuable improvements in our previous method of using geochemical variation diagrams. This new approach uses a ternary diagram that is subdivided into equally spaced segments along each of its three sides and has a triangular area in its center. The segments are assigned distinct colors that cover the range of the visible spectrum. The apexes are assigned the three primary colors, and the center triangle, which represents equal proportions of the three apexes, is assigned the color gray. The apexes are assigned the average Fe and $(Th/Ti)_c$ (ratio normalized to chondrites) compositions of KREEP/Mg-suite rocks, mare basalts, and ferroan anorthosites. The composition of each picture element (pixel) within these Apollo orbital gamma ray databases is used to determine its position within the ternary diagram. The color corresponding to this ternary position is then placed on a classification map at that pixel's position within the orbital databases. Error databases produced for the Fe and $(Th/Ti)_c$ data were used to exclude pixels having high errors. The resultant classification map shows spatial transitions among petrologic units, allows direct determination of the relative proportions of each end-member composition in a pixel, and increases the geologic interpretability of these data over that of the individual elemental databases. The classification units correspond remarkably well to observed geologic units, when we consider the spatial resolution (100 km) of the gamma ray spectrometer. Our results are as follows: (1) The highlands contain large areas of relatively pure ferroan anorthosite. (2) The average composition of the upper lunar crust is represented by an "anorthositic gabbro" composition, which supports the "magma-ocean" hypothesis for lunar crustal genesis. (3) KREEP/Mg-suite rocks are a minor fraction of the upper lunar crust. (4) Within the farside highlands, areas of KREEP/Mg-suite rocks coincide mostly with areas of crustal thinning, which are probably areas of KREEP basalt extrusions or localized excavations of Mg-suite rocks or KREEP-rich rocks. (5) Portions of the east limb and farside highlands have considerable amounts of a mafic, chondritic Th/Ti component (like mare basalt) whose occurrences coincide with mapped concentrations of light plains that display dark-halo craters; the presence of this component supports the hypothesis that mare volcanism had occurred within this highland region before the end of final heavy bombardment.

INTRODUCTION

We described last year a new method for direct comparison of lunar sample and orbital geochemical data using chemical variation diagrams that include Fe (wt %) versus $(Th/Ti)_c$, Mg* versus $(Th/Ti)_c$, and Al (wt %) versus Mg*/$(Th/Ti)_c$ [*Davis and Spudis*, 1985]. Mg* is equal to 100 Mg/Mg + Fe molar and $(Th/Ti)_c$ is the Th/Ti ratio normalized to Cl chondritic Th and Ti values. Within each variation diagram, we defined petrologic fields or units on the basis of coincidence of orbital and sample geochemical data and on the basis of obvious data clusters and mixing trends between rock types. For a particular diagram, the spatial distribution of its units on the moon was shown in map format by assigning a distinct color to the unit's pixels at their respective locations in the La Jolla Consortium databases. The orbital data for the maria were not included in our study because we were examining geochemical variations within the highlands for petrologic information that may provide new insights into highland crustal evolution [*Spudis and Davis*, 1985, 1986].

There are three disadvantages of the method presented last year. First, geochemical transitions between adjacent highland petrologic units on the classification maps were obscured by the units' color assignments; these particular assignments were dictated by the need to discriminate units of very small areal extent [see Plates 1 and 2, *Davis and Spudis*, 1985]. Second, the method was highly supervised; petrologic unit boundaries were first established within the variation diagrams on the basis of orbital-data correspondence to known rock types. The orbital data not yet classified by these boundaries were then classified by boundaries established at arbitrary intervals between the end-member boundaries. Thus the assignment of geochemical boundaries for each unit obscured important petrologic transition zones. In addition, the analyses did not consider the inherent errors in each of the orbital chemical databases. Third, the geochemical relations of the frontside maria and highlands could not be determined from the resultant classification maps because mare areas were excluded from those analyses. In order to overcome these limitations, we have devised a ternary-diagram approach that greatly increases not only the geologic interpretability, but also the reliability of the resultant classification maps.

Paper number 6B7230.

METHOD AND RESULTS

In this paper, we confine the presentation of our ternary-diagram analysis and subsequent discussion of the results to use of the Fe (wt %) versus $(Th/Ti)_c$ variation diagram, because these data include only the gamma ray orbital data, which have more global coverage (about 19%) than that of the X ray orbital data (about 9%; compare Plates 1 and 2 in *Davis and Spudis* [1985]). We produced an error database for Fe, Th, Ti, and $(Th/Ti)_c$ to take into account the analytical errors associated with the Fe and $(Th/Ti)_c$ data in the present analysis. This study used the Fe data of *Davis* [1980], the Th data of *Metzger et al.* [1977], and the Ti data of *Metzger and Parker* [1979]. Estimates of the Fe and $(Th/Ti)_c$ errors associated with each pixel in the databases were obtained by the standard method of determining error from counting statistics. This error is equal to the square root of the number of counts divided by the counting time (seconds). Generally, the longer the counting time,

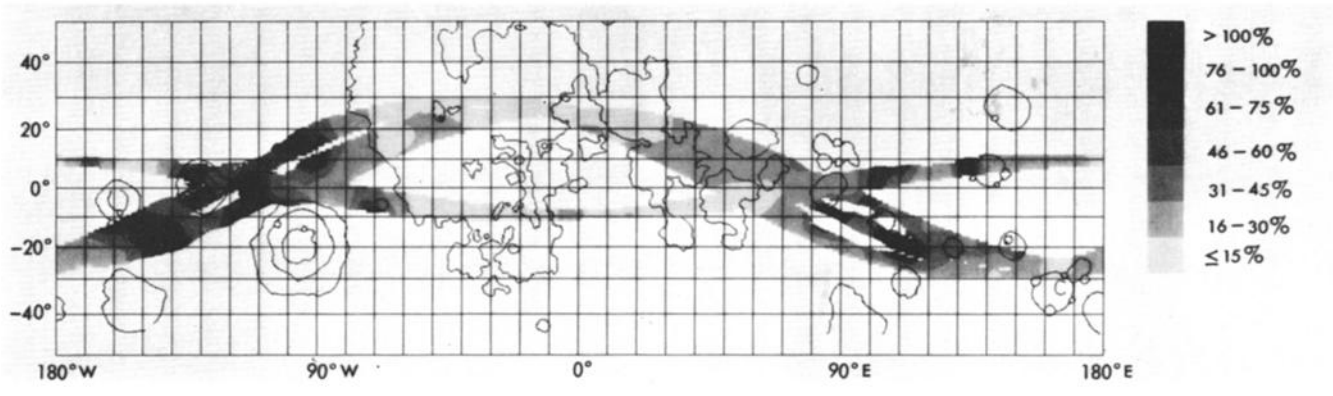

Fig. 1. Map of relative error in Apollo orbital gamma ray Fe data. See text for derivation.

the lower the error associated with the value. Each pixel's counting errors for Fe, Ti, and Th were calculated and the resulting errors in counts-per-second (cps) were converted to ppm (for Th) and wt % (for Ti and Fe); in this procedure we used each element's reported regression equation that relates cps to concentration [see *Metzger et al.*, 1977; *Metzger and Parker*, 1979; *Davis*, 1980, respectively]. The error associated with the $(Th/Ti)_c$ ratio was obtained by recalculating each pixel's ratio, considering its Th and Ti errors, and differencing this result by the pixel's original $(Th/Ti)_c$ ratio. Each pixel's errors for Fe and the $(Th/Ti)_c$ ratio were then placed in two new databases at the location of that pixel in the original elemental databases. The magnitude of the errors for Fe and $(Th/Ti)_c$ is shown in Figures 1 and 2, respectively, in which the values represent percent error relative to the concentration or concentration ratio of the pixel. Comparison of the Fe and $(Th/Ti)_c$ relative-error maps with the original elemental databases shows that areas of high relative error in Fe or $(Th/Ti)_c$ correspond to regions with low orbital accumulation times and with very low Fe or Ti concentrations, respectively. This relation also exists in tabulations of the regional data for Fe [*Davis*, 1980] and Ti [*Metzger and Parker*, 1979].

Although there are about 10 additional sources for error in the orbital chemical data [detailed in *Metzger et al.*, 1977], the counting statistics or orbital accumulation error generally constitutes 70–80% of the total error associated with each pixel's elemental values [see *Metzger et al.*, 1977; *Metzger and Parker*, 1979; *Davis*, 1980]. The only problem with this simple error analysis is underestimation of the $(Th/Ti)_c$ errors, because the nonthorium elemental contributions (e.g., U, K, Fe) to the Th cps are not accounted for in our error estimate for Th. However, this latter error amounts to only 6–8% of the regional Th concentrations [see Table 3 in *Metzger et al.*, 1977]. Thus, this slight underestimate in Th error will not affect the following analysis in which pixels that have large concentration errors are excluded from consideration in the ternary analysis.

The ternary-diagram approach outlined in this paper is an attempt to show as much detailed geochemical information as possible on a single map that indicates petrologic variations within the lunar crust. The method starts by establishing a ternary reference diagram whose three sides are each divided into eight segments; the two apical segments each represent 15% of a side's length and there are six equally spaced divisions between apexes (see Plate 1, top left). Thus each of the six intermediate segments represents about 12% of a side's length. Each ternary subdivision is assigned a distinct color; the colors represent a spectral continuum from red to green to blue to red. The center of the diagram is a triangular area representing approximately equal proportions of each apex, and it is thus assigned a gray color. The height of the central triangle represents the 25–50% range in relative proportions of the three apexes. Thus assignment of rock end-member compositions to the three apexes allows rock or soil compositions that are binary or ternary mixtures of these three end members to be represented as continuous colors in the visible spectrum.

Each of the end-member compositions is an average calculated from values reported in the literature [*Ryder and Norman*, 1978; *Ryder*, 1979; *Warren and Wasson*, 1979, 1980; *Basaltic Volcanism Study Project*, 1981; *Lofgren and Lofgren*, 1981; *Warren et al.*, 1981, 1983*a,b*]. After *Longhi and Boudreau* [1979], we normalized the Th/Ti ratio to Cl chondritic values (Ti = 430 ppm [*Mason*, 1971]; Th = 0.031 ppm [*Morgan*, 1971]).

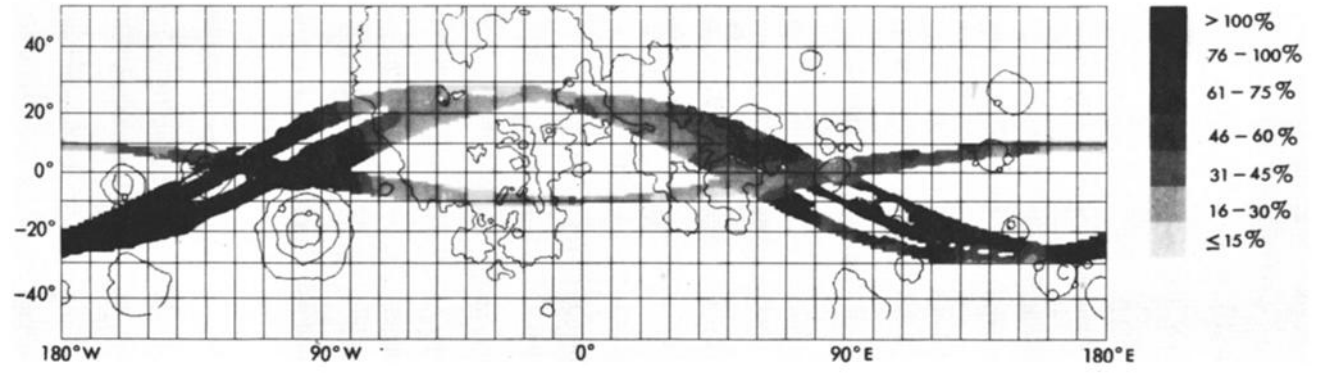

Fig. 2. Map of relative error in Apollo orbital gamma ray $(Th/Ti)_c$ data. See text for derivation.

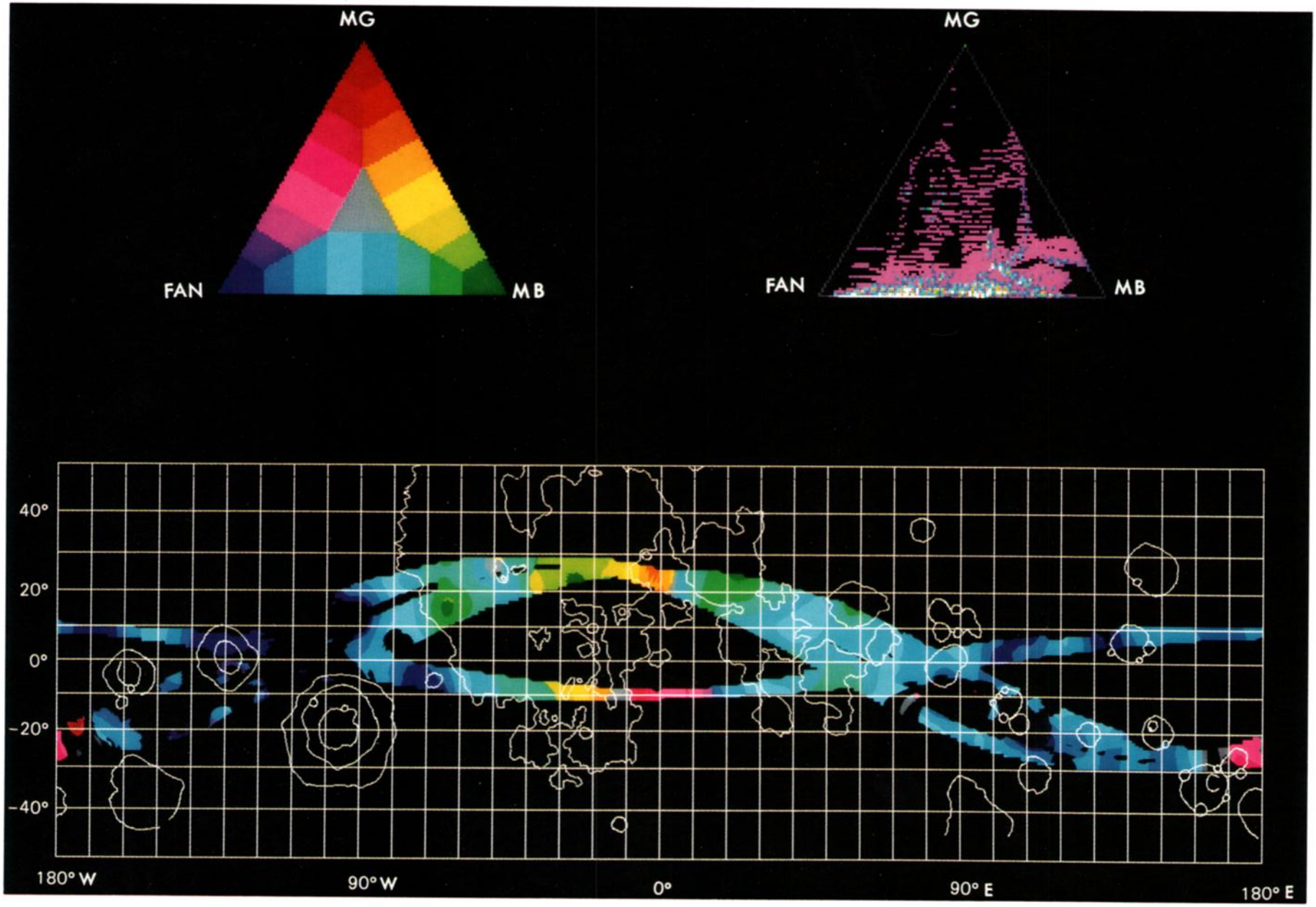

Plate 1. Ternary-diagram analysis of orbital Fe and $(Th/Ti)_c$ data in which pixels that have Fe or $(Th/Ti)_c$ errors greater than or equal to 75% are excluded. Top left: ternary reference diagram. Apex letter designation corresponds to Mg suite and KREEP (MG), mare basalt (MB), and ferroan anorthosite (FAN). Top right: ternary pixel scattergram. Color-pixel frequency correspondence is: magenta—less than or equal to 25, blue—50, cyan—75, green—100, yellow—125, red—150, bright red—175, and white—greater than or equal to 200. Bottom: petrologic classification unit map. Relative end-member compositions for each unit can be determined from ternary reference diagram (upper left).

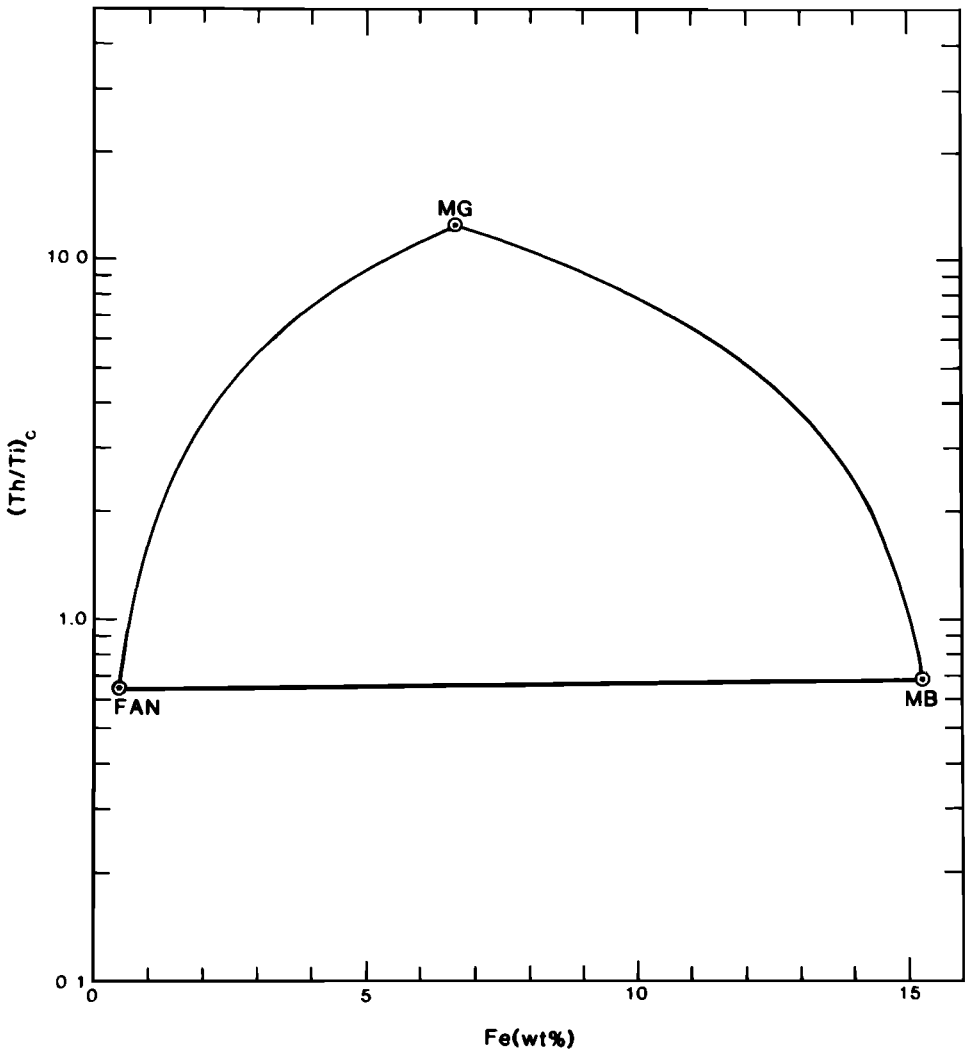

Fig. 3. Representation of the ternary diagram within the Fe versus $(Th/Ti)_c$ variation diagram, in which the apexes were assigned the average compositions of Mg-suite and KREEP rocks (MG), mare basalts (MB), and ferroan anorthosites (FAN). See text for apex values.

The location of the ternary boundaries formed by these three apical compositions within the Fe versus $(Th/Ti)_c$ diagram is shown in Figure 3. The Mg-suite (troctolite and norite) and KREEP rocks [Fe = 6.67 wt %, $(Th/Ti)_c = 12.37$] are represented by the red apex, the mare basalt [Fe = 15.28 wt %, $(Th/Ti)_c = 0.68$] by green, and the ferroan anorthosite [Fe = 0.5 wt %, $(Th/Ti)_c = 0.64$] by blue. Thus we can now assign a color from the ternary reference diagram to each pixel in the orbital geochemical databases using the Fe-concentration and $(Th/Ti)_c$-ratio values of the pixel and the ternary apexes. The relative proportion of each of the three compositional end members (apexes) needed to produce the observed composition of a particular pixel is obtained by (1) finding the point of intersection (PI) of a line formed by a particular apex (A_n) and the pixel with the side of the ternary that is opposite to A_n; (2) calculating the calculating the distance (D) between PI and A_n; (3) calculating the distance (d) between the pixel and PI; and (4) calculating the ratio d/D, which represents the proportion of that apical composition (A_n) in the pixel's composition. Thus if a pixel falls on the side of the diagram, the contribution of the opposite apical composition is zero; i.e., the pixel is a binary mixture of the two other end-member compositions. Likewise, a pixel that falls on an apex consists only of that apical composition. Any pixel that falls within the ternary borders consists of a mixture of the three end-member compositions. The sum of the relative contributions of the three end members to a pixel's composition is 100%; thus the contributions of only two components are needed to locate the pixel within the ternary reference diagram. Once the pixel's location within the diagram has been determined, the color at that location in the reference ternary is assigned to that pixel's position in a new image or map file. This process is then repeated for every pixel within the orbital databases. The resultant color-classification map shows (1) the relative contributions of the three end-member compositions over the entire orbital groundtracks of Apollo 15 and 16, and (2) the transitional nature of these geochemical or petrologic units (Plate 1).

At the same time as ternary color assignments are made to each pixel, the frequencies of occurrence of pixels at a particular ternary composition are accumulated within a ternary scattergram (e.g., Plate 1, top right). This scattergram shows the relative areal proportions of ternary compositions within the Apollo 15 and 16 groundtracks.

Certain pixel areas within the Fe and $(Th/Ti)_c$ databases have

TABLE 1. Areal and Chemical Characteristics of Geochemical Units on Fe-$(Th/Ti)_c$ Classification Map

Unit*	Area† (10^3 km^2)	Area Percent Groundtrack	Area Percent Moon	Fe (wt %) Mean±σ	Fe Error (wt %) Mean±σ	$(Th/Ti)_c$ Mean±σ	$(Th/Ti)_c$ Error Mean±σ	Ternary Coordinates‡ (Percent)		
								MG	MB	FAN
1	14	0.25	0.04	5.7 ± 1.1	1.9 ± 0.8	20.73 ± 14.3	16.96 ± 3.50	97	1	2
3	12	0.21	0.03	9.4 ± 0.4	1.1 ± 0.1	7.88 ± 0.34	2.41 ± 0.27	61	35	4
4	51	0.89	0.13	9.2 ± 0.7	1.0 ± 0.2	6.45 ± 0.72	1.67 ± 0.47	49	39	12
5	43	0.75	0.11	10.4 ± 0.5	1.0 ± 0.1	5.04 ± 0.64	1.00 ± 0.12	37	52	11
6	65	1.14	0.17	11.1 ± 0.4	1.1 ± 0.2	3.30 ± 0.43	0.59 ± 0.12	23	62	15
7	97	1.69	0.25	12.8 ± 0.6	1.2 ± 0.2	2.54 ± 0.30	0.43 ± 0.10	16	76	8
8	31	0.54	0.08	13.7 ± 0.6	1.5 ± 0.3	1.52 ± 0.80	0.35 ± 0.08	8	85	7
9	222	3.88	0.58	12.0 ± 0.4	1.6 ± 0.2	1.16 ± 0.44	0.31 ± 0.06	5	76	19
10	546	9.54	1.44	10.3 ± 0.5	1.4 ± 0.3	1.42 ± 0.70	0.34 ± 0.13	8	63	29
11	733	12.79	1.93	8.9 ± 0.5	1.5 ± 0.3	1.23 ± 0.75	0.40 ± 0.18	7	54	39
12	546	9.53	1.44	6.8 ± 0.5	1.5 ± 0.4	1.10 ± 0.72	0.56 ± 0.40	6	41	53
13	1086	18.96	2.86	5.2 ± 0.4	1.4 ± 0.4	0.73 ± 0.47	0.42 ± 0.30	3	32	65
14	935	16.33	2.46	3.7 ± 0.4	1.4 ± 0.4	0.67 ± 0.40	0.53 ± 0.39	2	22	76
15	981	17.12	2.58	2.1 ± 0.6	1.6 ± 1.0	0.56 ± 0.34	0.46 ± 0.26	2	12	86
16	19	0.33	0.05	2.9 ± 0.5	1.7 ± 0.5	2.41 ± 0.42	2.02 ± 1.21	16	11	73
17	13	0.22	0.03	4.4 ± 0.7	1.1 ± 0.7	3.40 ± 0.56	1.90 ± 1.81	24	18	58
18	88	1.53	0.23	5.2 ± 1.0	1.2 ± 0.7	4.91 ± 0.52	2.74 ± 1.59	37	18	45
19	79	1.37	0.21	6.1 ± 0.7	1.1 ± 0.3	6.02 ± 0.56	4.83 ± 2.77	46	20	34
20	26	0.45	0.07	6.2 ± 0.4	1.1 ± 0.2	7.48 ± 0.47	7.21 ± 6.37	58	16	26
21	5	0.09	0.01	6.3 ± 0.3	1.3 ± 0.4	9.61 ± 0.50	5.20 ± 0.67	76	9	15
22	137	2.39	0.36	7.5 ± 0.8	1.2 ± 0.3	4.75 ± 0.93	3.32 ± 2.78	36	33	31
Global	5729	100.00	15.06	6.2 ± 0.5	1.4 ± 0.5	1.37 ± 0.57	0.72 ± 0.43	8	36	56

Classification map is not shown in this paper. Pixels that have errors greater than or equal to 250% in $(Th/Ti)_c$ are excluded.
*See Figure 4 for unit number versus ternary unit correspondence; unit 2 excluded because no orbital data fall within it.
†Calculated using an area of 57.54 km^2 for each 1/4° pixel.
‡Values represent average end-member proportions for pixels falling within each ternary unit.

high uncertainties (Figures 1 and 2), that is, the areal representation of units that contain these unreliable pixels on the classification map is questionable. Because these high uncertainties generally correspond to pixels with very low concentrations of either Fe or Ti, units with the lowest degree of reliability with respect to areal abundance probably represent rock compositions having either low Fe (such as ferroan anorthosites) or low Ti (such as the Mg suite). To determine the effects of these errors on the areal abundance of units within the classification map, we decreased by increments the amount of error that pixels could have in terms of Fe and $(Th/Ti)_c$ before being excluded from the classification map. A product of this exclusion process is shown in Plate 1, where the error limit for both Fe and $(Th/Ti)_c$ databases was set at 75%. This level of error exclusion provides a reasonable amount of certainty for the remaining unit pixels and their areal abundances.

The effect of error exclusion in the ternary analysis of Fe versus $(Th/Ti)_c$ is shown by comparing Tables 1 and 2. Table 1 represents an error exclusion of greater than or equal to 250% on only the $(Th/Ti)_c$ data and, as such, has eliminated very few data from the Apollo groundtracks (0.6 areal percent; map not shown). Table 2 represents an error exclusion of greater than or equal to 75% on both the Fe and $(Th/Ti)_c$ data, in which about 25% of the orbital groundtrack has been excluded (map, Plate 1). Comparison of the data in these two tables shows: (1) that the average unit errors for both Fe and $(Th/Ti)_c$ data have decreased from Table 1 to Table 2, as expected; (2) that the areal abundances of unit 1 and units 12 through 20 have decreased the most in the 75% error exclusion because of a combination of the high relative errors associated with the low Ti concentrations in those units trending toward the MG apex; and (3) that even with the reduction in areas of these units, their average Fe and $(Th/Ti)_c$ concentrations have not changed significantly. We feel that the classification map (Plate 1), because it excludes pixels that have Fe and $(Th/Ti)_c$ errors greater than or equal to 75%, provides a reasonably reliable database for geologic interpretation.

The two units representing the apical compositions of the MG (unit 1) and FAN (unit 15) end members have $(Th/Ti)_c$ values that fall just outside the ternary diagram. This is to be expected because the ternary apexes are defined by average rock compositions: there are samples and pixels that fall either above or below these average $(Th/Ti)_c$ values. However, the pixels that do plot outside the ternary are a very minor fraction of the total data and they fall close to the ternary borders. The ternary coordinates of these pixels were determined by collapsing each pixel onto the nearest ternary border in an orthogonal direction to that border.

DISCUSSION

Examination of the classification map allows easy determination of (1) the global spatial distribution of end-member compositions, (2) the transitional spatial relations between end-member compositions, and (3) quantitative estimates of the relative proportions of each end member at each pixel location within the orbital groundtracks. The classification map also demonstrates two additional advantages of this technique over previous analytical methods that used orbital geochemical data for geologic interpretation. First, the method uses and shows the chemical information from three elements: the number of elements is limited only by the number of available orbital databases and the ingenuity of the analyst in devising elemental ratios and/or combinations for the apical compositions, which serve as petrologic discriminators. We have, in fact, used up to five elements in our previous analyses [*Davis and Spudis*, 1985], but two of these elements (Al and Mg) were from X ray databases, which provide less surface coverage than the

TABLE 2. Areal and Chemical Characteristics of Geochemical Units on Fe-$(Th/Ti)_c$ Classification Map

Unit*	Area† (10^3 km^2)	Area Percent Groundtrack	Area Percent Moon	Fe (wt %) Mean±σ	Fe Error (wt %) Mean±σ	$(Th/Ti)_c$ Mean±σ	$(Th/Ti)_c$ Error Mean±σ	Ternary Coordinates‡ (Percent)		
								MG	MB	FAN
1	6	0.14	0.02	6.2 ± 0.1	1.3 ± 0.1	13.01 ± 1.36	8.16 ± 0.38	96	1	3
3	12	0.27	0.03	9.4 ± 0.4	1.1 ± 0.1	7.88 ± 0.34	2.41 ± 0.27	61	35	4
4	51	1.16	0.13	9.2 ± 0.7	1.0 ± 0.2	6.45 ± 0.72	1.67 ± 0.47	49	39	12
5	43	0.98	0.11	10.4 ± 0.5	1.0 ± 0.1	5.04 ± 0.64	1.00 ± 0.12	37	52	11
6	65	1.49	0.17	11.1 ± 0.4	1.1 ± 0.2	3.30 ± 0.43	0.59 ± 0.12	23	62	15
7	97	2.20	0.25	12.8 ± 0.6	1.2 ± 0.2	2.54 ± 0.30	0.43 ± 0.10	16	76	8
8	31	0.71	0.08	13.7 ± 0.6	1.5 ± 0.3	1.52 ± 0.80	0.35 ± 0.08	8	85	7
9	222	5.04	0.58	12.0 ± 0.4	1.6 ± 0.2	1.16 ± 0.44	0.31 ± 0.06	5	76	19
10	546	12.43	1.44	10.3 ± 0.5	1.4 ± 0.3	1.42 ± 0.70	0.34 ± 0.13	8	63	29
11	732	16.66	1.93	8.9 ± 0.5	1.5 ± 0.3	1.23 ± 0.74	0.39 ± 0.16	7	54	39
12	474	10.79	1.25	6.9 ± 0.5	1.4 ± 0.4	1.01 ± 0.54	0.40 ± 0.15	5	42	53
13	928	21.14	2.45	5.2 ± 0.4	1.3 ± 0.4	0.71 ± 0.42	0.32 ± 0.11	3	32	65
14	579	13.19	1.53	3.8 ± 0.4	1.3 ± 0.4	0.66 ± 0.36	0.30 ± 0.11	2	23	75
15	370	8.43	0.98	2.3 ± 0.4	1.2 ± 0.3	0.57 ± 0.25	0.26 ± 0.09	1	14	85
16	15	0.33	0.04	2.9 ± 0.5	1.6 ± 0.4	2.43 ± 0.41	1.53 ± 0.30	16	11	73
17	9	0.21	0.02	4.3 ± 0.3	0.9 ± 0.6	3.28 ± 0.46	0.95 ± 0.56	23	18	59
18	70	1.60	0.19	5.5 ± 0.7	0.9 ± 0.2	4.92 ± 0.51	2.26 ± 0.82	37	19	44
19	40	0.91	0.11	5.8 ± 0.7	1.0 ± 0.1	6.05 ± 0.62	3.02 ± 1.19	46	17	37
20	15	0.34	0.04	6.1 ± 0.4	1.1 ± 0.2	7.57 ± 0.53	2.51 ± 0.87	59	14	27
21	5	0.11	0.01	6.4 ± 0.1	1.2 ± 0.1	9.59 ± 0.50	5.04 ± 0.11	75	10	15
22	82	1.87	0.22	7.8 ± 0.9	1.2 ± 0.3	4.45 ± 0.81	1.69 ± 0.97	33	36	31
Global	4392	100.00	11.58	7.0 ± 0.5	1.4 ± 0.3	1.38 ± 0.52	0.48 ± 0.17	8	42	50

Classification map shown in Plate 1. Pixels that have errors greater than or equal to 75% in Fe and $(Th/Ti)_c$ are excluded.
*See Figure 4 for unit number versus ternary unit correspondence; unit 2 excluded because no orbital data fall within it.
†Calculated using an area of 57.54 km^2 for each 1/4° pixel.
‡Values represent average end-member proportions for pixels falling within each ternary unit.

gamma ray data. Second, the use of elemental ratios in our analyses, instead of the commonly used elemental bivariate diagrams [e.g., *Clark et al.*, 1978; *Clark and Hawke*, 1981], shows geologic information that is otherwise hidden in individual elemental databases. This point is clearly demonstrated by comparison of our classification map with the Fe, Ti, and Th elemental maps along the Apollo 16 groundtrack from Mare Cognitum to Mare Nectaris. For this region, the Fe map [*Davis*, 1980], Ti map [discussed but not shown in *Metzger and Parker*, 1979; see *Davis*, 1980], and Th map [*Frontispiece*, 1977] show only regional gradations in elemental concentrations. However, our classification map, based on Fe and the $(Th/Ti)_c$ ratio, shows geologic diversity within the same region and corresponds remarkably well with its geology. Plate 1 shows the transition from mare basalt (in western Oceanus Procellarum) to a KREEP-mare-basalt region (at Mare Cognitum), to an area that represents a mixture of all three end-member compositions (the thin mare basalts between Fra Mauro and Ptolemaeus), to a mixed Mg-suite/ferroan anorthosite zone (from the border of Mare Nubium across the central highlands), to a relatively pure ferroan anorthosite zone (near the Apollo 16 landing site). Thus considering the low resolution (100 km) of the gamma ray spectrometer, this ternary analysis has accurately reproduced the mapped geologic units within this orbital swath.

The Apennine Bench region is shown to have a composition corresponding to a mixture of KREEP and mare basalt, consistent with the results of previous studies [*Hawke and Head*, 1978; *Spudis*, 1978]. Other areas of Mg-suite/KREEP material are in the farside highlands near Van de Graaff (18°–29°S, 175°–171°W, Plate 1), within the Hertzsprung basin (3°–5°S, 125°–130°W), and south of Mare Smythii and west of Pasteur Crater (7°–15°S, 76°–98°E). The latter two areas are mostly excluded at the 75% error limit (Plate 1), but they can be easily distinguished on maps (not shown) with error exclusion down to the 100% level. The first two of these KREEP-rich highland areas coincide with areas of highland crustal thinning shown on the crustal thickness map [*Frontispiece*, 1976] of *Bills and Ferrari* [1977] that are covered by the orbital gamma ray data. An inverse relation between Th concentration and highland crustal thickness has been reported by *Metzger et al.* [1977]. The preliminary elemental concentrations obtained by *Metzger et al.*, [1974] suggest that the Van de Graaff region may have a "granitic" rock composition, similar to that of sample 12013. Generally, the average composition of lunar granites is lower in Fe, Ti, and Mg and significantly higher in K and Th than that of KREEP basalts. The Fe and Ti concentrations of these three highland areas are indeed lower than that at any of the three nearside high-KREEP areas, possibly because of the proximity of maria to the KREEP-rich areas; however, the three highland KREEPy areas do not appear to be associated with extensive mare deposits. The X ray orbital data do not allow this comparison to be made for Mg. For K, *Parker et al.* [1981] have presented preliminary gamma ray data showing the Van de Graaff region to have only 880 ppm K, whereas they report the Fra Mauro region as having 2680 ppm K. This significantly lower K value for Van de Graaff strongly suggests that these KREEP/Mg-suite highland areas (at least that near Van de Graaff) are not composed of "granitic" rock. They are most likely either "KREEPy basalts" [*Hawke and Spudis*, 1980] resulting from volcanism propagated by crustal thinning in these areas, or the remnants of an Mg-suite pluton exposed by an early impact event (such as the South Pole-Aitken basin; *Wilhelms* [1984]).

Our classification map also shows that, at the spatial resolution (about 100 km) of the gamma ray instrument, the central regions of most major maria have relatively pure mare-basalt compositions. Only Mare Tranquillitatis appears to have compositions transitional between mare basalt and ferroan

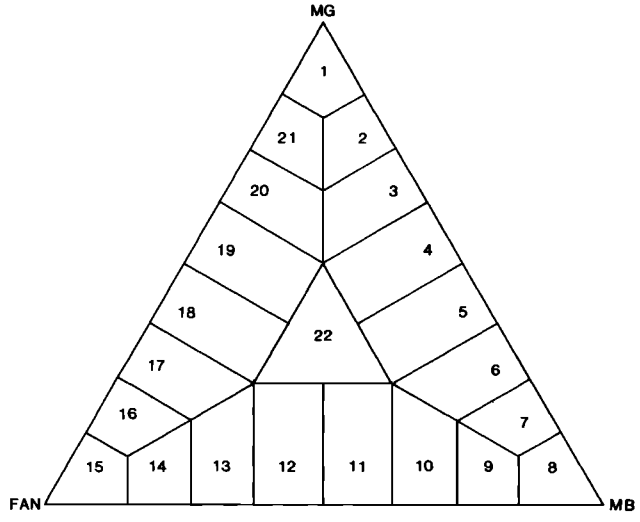

Fig. 4. Petrologic unit number designation for color segments within the ternary reference diagram.

anorthosite. Within Mare Tranquillitatis, such a composition would probably result from the addition of underlying anorthositic highlands debris to mare-basalt regoliths by vertical mixing through relatively thin, young, blue mare-basalt flows [*Hörz*, 1978; *Whitford-Stark and Head*, 1980]. At Aristarchus, the unit map indicates a mixture of KREEP, mare basalt, and ferroan anorthosite (gray unit), which grades into a more KREEP- and mare-basalt-rich unit (yellow) at the north border of the groundtrack (Plate 1). The presence of these two units can be attributed to the relatively thin, young, blue mare-basalt flows in these two areas [*Pieters*, 1978] that mixed with underlying KREEP- or Mg-suite-rich highland terrain. This underlying material is present at relatively shallow depth, as indicated by its exposure within Aristarchus Crater [*McCord et al.*, 1972; *Guest and Spudis*, 1985].

A series of relatively young lava flows with well-developed flow fronts occur in southwestern Mare Imbrium [*Schaber*, 1973]. In addition to their striking morphological development, remote-sensing data indicate that these lava flows are rich in Ti [*Pieters*, 1978], relatively rich in Th (8.0 ppm; *Etchegaray-Ramirez et al.* [1983]), and young (less than 2.0 b.y. old; *Schultz and Spudis* [1983]). These high-Ti, KREEP-rich lavas are represented on our petrologic map as a small patch of unit 6 (Figure 4; Plate 1, top left) that appears near 20°–25°N, 35°–40°W (Plate 1) and larger regions of unit 7 that extend well into Mare Imbrium. Our ability to identify these flows on the petrologic map suggests that individual mare-basalt flows, particularly those that are geochemically anomalous, will be mappable from future global gamma ray data.

Another interesting area is within and near the Balmer basin on the lunar eastern limb. A zone of unit 22 (gray; Plate 1) occurs at about 10°–15°S, 75°E. The position of this zone of unit 22 correlates with the light plains fill of the Balmer basin, which has been described previously as KREEP-rich, mare-like deposits [*Hawke and Spudis*, 1980; *Hawke et al.*, 1985]. Our classification map (Plate 1) shows these plains to represent roughly an equal mixture of anorthosite, mare basalt, and KREEP/Mg-suite material. The identification of dark-halo craters in this region [*Schultz and Spudis*, 1979; *Hawke et al.*, 1985] supports the suggestion that light plains in the region thinly mantle buried, KREEP-rich mare-basalt flows. These basalt flows are probably older than 3.9 b.y. because they are buried by highland plains of Imbrian to Nectarian age [*Wilhelms and El-Baz*, 1977]. It thus appears that the ancient lunar maria (older than 3.9 b.y.) had a diversity of chemical compositions, ranging from "normal" chondritic Th/Ti values to more KREEP-rich varieties.

The lunar surface represented by the Apollo orbital groundtracks is shown in Plate 1 and Table 2 to consist of 8.4% relatively pure (85%) ferroan anorthosite (unit 15), even by exclusion of pixels with high compositional uncertainties. Deleting the maria from these data raises this value to 12.9%. Most of the lunar highlands is composed of units 12 through 15 (Figure 4, Plate 1). Considering the areal percentages of the groundtracks and the modal amounts of the end-member components for these four units results in an average highland composition of 68% ferroan anorthosite, 29% mare basalt, and 3% KREEP/Mg-suite rocks. Our exclusion from this calculation of some of the highlands KREEP-rich units causes the proportion of KREEP/Mg-suite rocks to be a little low; it is not, however, significantly lower than our previous estimate [*Davis and Spudis*, 1985] because of the small areal extent of the units having greater amounts of the MG component (units 16 through 21, Table 2). This resultant rock composition approximates that of "anorthositic gabbro" and is consistent with our previous analyses [*Davis and Spudis*, 1985]. This composition may represent the average composition of the upper half of the highlands crust [*Spudis and Davis*, 1986].

Significant amounts of mare basalt (21.1% of the Apollo groundtrack) occur within the highlands (mostly on the eastern limb and farside highlands), as indicated by the areal distribution of unit 13 (Figure 4, Plate 1). This unit is composed of 65% ferroan anorthosite, 3% KREEP/Mg suite, and 32% mare basalt (Table 2). Its areal distribution coincides with mapped occurrences of highland plains that display dark-halo craters [*Schultz and Spudis*, 1979, 1983], for which spectral data indicate the presence of excavated mare basalt [*Hawke and Bell*, 1981]. This coincidence suggests that mare volcanism occurred within these highland areas before the end of the final heavy bombardment. Additional lines of evidence are listed in *Davis and Spudis* [1985]. We do not, however, dismiss the possibility that this unit may represent some type of highland gabbro or a mixture of Mg-suite rocks with an as yet unsampled mafic rock type that has a subchondritic Th/Ti ratio.

CONCLUSION

We have presented an improved method for global petrologic mapping on the moon. This method employs a color-coded ternary diagram whose apexes are assigned rock end-member compositions. Using these compositions and the composition of each pixel within the orbital gamma ray data, we can display the distribution of the continuum of rock compositions that occur on the lunar surface. Error databases for Fe and the $(Th/Ti)_c$ ratio have also been generated in this study and are used to exclude pixels with high error. The resultant classification map allows rapid quantitative determination of each pixel's composition in terms of the three end-member compositions. The map also shows the lateral transitional nature of each of the resultant petrologic units. This technique provides more geologic information than can be obtained by using only the elemental data. The map units correspond remarkably well with previously delineated geologic provinces.

Our findings from this analysis do not differ significantly from those that we obtained last year by a more supervised approach:

1. The average crustal composition of the upper highlands is similar to that of "anorthositic gabbro." This composition is more consistent with the "magma-ocean" concept of large-scale plagioclase fractionation for lunar crustal origin than with the serial magmatism hypothesis [see also *Spudis and Davis*, 1986].

2. Portions of the east-limb and farside highlands have considerable amounts of a mafic, chondritic Th/Ti component, not unlike mare basalt. The correspondence of these petrologic units with mapped occurrences of dark-halo craters lends credence to the hypothesis that mare volcanism had occurred within these highland terrains before the end of the heavy bombardment.

3. Three areas within the highlands are represented by petrologic units having a high proportion of a KREEP/Mg-suite rock component. Two of these occurrences coincide with areas of highland crustal thinning, and they probably represent extrusions of KREEP basalt or localized excavations of Mg-suite rocks or KREEP-rich rocks. Orbital potassium data preclude their compositional relation to granitic rock.

4. There is very good correspondence between observed geologic units and our classification units along the Apollo 16 groundtrack from western Oceanus Procellarum to Mare Nectaris; this correspondence is not observed on the Fe, Ti, or Th elemental maps. Our classification map also discriminates a young, Ti- and Th-rich lava flow from the surrounding basalt flows in southwestern Mare Imbrium; this flow cannot be so distinguished on the elemental maps. We are convinced that the use of three elements in the analysis has enabled our method to discriminate geologic units on the moon with greater precision than have previous methods that restricted bivariate analysis to only two elements.

Acknowledgments. This paper has benefited greatly from the critical review by A. E. Metzger. The authors also thank J. Bell and G. Swann for their review comments. This work was supported by NASA Planetary Geology Program contract W13,709.

REFERENCES

Basaltic Volcanism Study Project, *Basaltic Volcanism on the Terrestrial Planets*, 1286 pp., Pergamon, New York, 1981.

Bills, B. G., and A. J. Ferrari, A lunar density model consistent with topographic, gravitational, librational, and siesmic data, *J. Geophys. Res., 82*, 1306–1314, 1977.

Clark, P. E., and B. R. Hawke, Compositional variation in the Hadley Apennine region, *Proc. Lunar Planet. Sci. 12B*, 727–749, 1981.

Clark, P. E., E. M. Eliason, C. G. Andre, and I. Adler, A new color correlation method applied to XRF Al/Si ratios and other lunar remote sensing data, *Proc. Lunar Planet. Sci. Conf. 9th*, 3015–3027, 1978.

Davis, P. A., Iron and titanium distribution on the moon from orbital gamma ray spectrometry with implications for crustal evolutionary models, *J. Geophys. Res., 85*, 3209–3224, 1980.

Davis, P. A., and P. D. Spudis, Petrologic mapping of the lunar highlands derived from orbital geochemical data, *Proc. Lunar Planet. Sci. Conf. 16th*, in *J. Geophys. Res., 90*, D61–D74, 1985.

Etchegaray-Ramirez, M. I., A. E. Metzger, E. L. Haines, and B. R. Hawke, Thorium concentrations in the lunar surface: IV. Deconvolution of the Mare Imbrium, Aristarchus and adjacent regions, *Proc. Lunar Planet. Sci. Conf. 13th*, in *J. Geophys. Res., 88*, A529–A543, 1983.

Frontispiece, *Proc. Lunar Sci. Conf. 7th*, v. 1, Plate 3, 1976.

Frontispiece, *Proc. Lunar Sci. Conf. 8th*, v. 1, Plate 1, 1977.

Guest, J. E., and P. D. Spudis, The Aristarchus impact event and the effects of target material, *Geol. Mag., 122*, 317–327, 1985.

Hawke, B. R., and J. F. Bell, Remote sensing studies of lunar dark halo craters: Preliminary results and implications for early volcanism, *Proc. Lunar Planet. Sci. 12B*, 665–678, 1981.

Hawke, B. R., and J. W. Head, Lunar KREEP volcanism: Geologic evidence for history and mode of emplacement, *Proc. Lunar Planet. Sci. Conf. 9th*, 3285–3309, 1978.

Hawke, B. R., and P. D. Spudis, Geochemical anomalies on the eastern limb and farside of the moon, *Proc. Conf. Lunar Highlands Crust*, edited by J. J. Papike and R. B. Merrill, pp. 467–481, Pergamon, New York, 1980.

Hawke, B. R., P. D. Spudis, and P. E. Clark, The origin of selected lunar geochemical anomalies: Implications for early volcanism and the formation of light plains, *Earth Moon and Planets, 32*, 257–273, 1985.

Hörz, F., How thick are lunar mare basalts?, *Proc. Lunar Planet. Sci. Conf. 9th*, 3311–3331, 1978.

Lofgren, G. E., and E. M. Lofgren, *Catalog of Lunar Mare Basalts Greater Than 40 Grams*, Lunar and Planetary Institute Contribution 438, Lunar and Planetary Institute, Houston, 1981.

Mason, B., Titanium, in *Handbook of Elemental Abundances in Meteorites*, edited by B. Mason, pp. 181–184, Gordon and Breach, New York, 1971.

McCord, T. B., M. P. Charette, T. V. Johnson, L. A. Lebofsky, and C. Pieters, Lunar spectral types, *J. Geophys. Res., 77*, 1349–1359, 1972.

Metzger, A. E., and R. E. Parker, The distribution of titanium on the lunar surface, *Earth Planet. Sci. Lett., 45*, 155–171, 1979.

Metzger, A. E., E. L. Haines, R. E. Parker, and R. G. Radocinski, Thorium concentrations in the lunar surface. I: Regional values and crustal content, *Proc. Lunar Sci. Conf. 8th*, 949–999, 1977.

Metzger, A. E., J. I. Trombka, R. C. Reedy, and J. R. Arnold, Element concentrations from lunar orbital gamma-ray measurements, *Proc. Lunar Sci. Conf. 5th*, 1067–1078, 1974.

Morgan, J. W., Thorium, in *Handbook of Elemental Abundances in Meteorites*, edited by B. Mason, pp. 517–528, Gordon and Breach, New York, 1971.

Parker, R. E., E. L. Haines, and A. E. Metzger, Potassium concentrations in the lunar surface (abstract), in *Lunar and Planetary Science XII*, pp. 811–812, Lunar and Planetary Institute, Houston, 1981.

Pieters, C., Mare basalt types on the frontside of the moon: A summary of spectral reflectance data, *Proc. Lunar Planet. Sci. Conf. 9th*, 2825–2849, 1978.

Ryder, G., The chemical components of highlands breccias, *Proc. Lunar Planet. Sci. Conf. 10th*, 561–581, 1979.

Ryder, G., and M. Norman, *Catalogs of Pristine Non-Mare Rocks*, NASA JSC-14565 and -14603, NASA/Johnson Space Center, Houston, 1978.

Schaber, G. G., Lava flows in Mare Imbrium: Geologic evaluation from Apollo orbital photography, *Proc. Lunar Sci. Conf. 4th*, 72–93, 1973.

Schultz, P. H., and P. D. Spudis, Evidence for ancient mare volcanism, *Proc. Lunar Planet. Sci. Conf. 10th*, 2899–2918, 1979.

Schultz, P. H., and P. D. Spudis, The beginning and end of lunar mare volcanism, *Nature, 302*, 233–236, 1983.

Spudis, P. D., Composition and origin of the Apennine Bench Formation, *Proc. Lunar Planet. Sci. Conf. 9th*, 3379–3394, 1978.

Spudis, P. D., and P. A. Davis, How much anorthosite in the lunar crust?: Implications for lunar crustal origin (abstract), in *Lunar and Planetary Science XVI*, pp. 807–808, Lunar and Planetary Institute, Houston, 1985.

Spudis, P. D., and P. A. Davis, A chemical and petrological model of the lunar crust, *Proc. Lunar Planet. Sci. Conf. 17th*, in *J. Geophys. Res., 91*, E84–E90, 1986.

Warren, P. H., and J. T. Wasson, The compositional-petrographic search for pristine nonmare rocks: Third foray, *Proc. Lunar Planet. Sci. Conf. 10th*, 583–610, 1979.

Warren, P. H., and J. T. Wasson, Further foraging for pristine nonmare rocks: Correlations between geochemistry and longitude, *Proc. Lunar Planet. Sci. Conf. 11th*, 431–470, 1980.

Warren, P. H., G. J. Taylor, K. Keil, C. Marshall, and J. T. Wasson, Foraging westward for pristine nonmare rocks: Complications for petrogenetic models, *Proc. Lunar Planet. Sci. 12B*, 21–40, 1981.

Warren, P. H., G. J. Taylor, K. Keil, G. W. Kallemeyn, P. S. Rosenev, and J. T. Wasson, Sixth foray for pristine nonmare rocks and an assessment of the diversity of lunar anorthosites, *Proc. Lunar Planet. Sci. Conf. 13th*, in *J. Geophys. Res., 88*, A615–A630, 1983*a*.

Warren, P. H., G. J. Taylor, K. Keil, G. W. Kallemeyn, D. N. Shirley, and J. T. Wasson, Seventh foray: Whitlockite-like lithologies, a diopside-bearing troctolitic anorthosite, ferroan anorthosites and KREEP, *Proc. Lunar Planet. Sci. Conf. 14th*, in *J. Geophys. Res.*, *88*, B151–B164, 1983*b*.

Whitford-Stark, J. F., and J. W. Head, Stratigraphy of Oceanus Procellarum basalts: Sources and styles of emplacement, *J. Geophys. Res.*, *85*, 6579–6609, 1980.

Wilhelms, D. E., Moon, in *The Geology of the Terrestrial Planets*, edited by M. H. Carr, pp. 106–205, NASA SP-469, 1984.

Wilhelms, D. E., and F. El-Baz, Geologic map of the east side of the Moon, *U. S. Geological Survey Map I-948*, 1977.

P. A. Davis and P. D. Spudis, Branch of Astrogeology, U. S. Geological Survey, 2255 N. Gemini Dr., Flagstaff, AZ 86001.

(Received April 29, 1986;
revised October 10, 1986;
accepted November 13, 1986.)